Injection locking and coupling the emitters of large VCSEL arrays via diffraction in an external cavity

MORITZ PFLÜGER,[1] DANIEL BRUNNER,[2,*] TOBIAS HEUSER,[3] JAMES A. LOTT,[3] STEPHAN REITZENSTEIN,[3] AND INGO FISCHER[1]

[1]*Instituto de Física Interdisciplinar y Sistemas Complejos, IFISC (UIB-CSIC), Campus Universitat de les Illes Balears, Ctra. de Valldemossa km. 7.5, 07122 Palma, Spain*
[2]*FEMTO-ST/Optics Department, UMR CNRS 6174, Université de Franche-Comté/CNRS, 15B avenue des Montboucons, 25030 Besançon Cedex, France*
[3]*Institut für Festkörperphysik, Technische Universität Berlin, Hardenbergstraße 36, 10623 Berlin, Germany*
[*]*daniel.brunner@femto-st.fr*

Abstract: Networks of semiconductor lasers are the foundation of numerous applications and fundamental investigations in nonlinear dynamics, material processing, lighting, and information processing. However, making the usually narrowband semiconductor lasers within the network interact requires both high spectral homogeneity and a fitting coupling concept. Here, we report how we use diffractive optics in an external cavity to experimentally couple vertical-cavity surface-emitting lasers (VCSELs) in a 5×5 array. Out of the 25 lasers, we succeed to spectrally align 22, all of which we lock simultaneously to an external drive laser. Furthermore, we show the considerable coupling interactions between the lasers of the array. This way, we present the largest network of optically coupled semiconductor lasers reported so far and the first detailed characterization of such a diffractively coupled system. Due to the high homogeneity of the lasers, the strong interaction between them, and the scalability of the coupling approach, our VCSEL network is a promising platform for experimental investigations of complex systems, and it has direct applications as a photonic neural network.

1. Introduction

Semiconductor lasers (SLs) are particularly sensitive to optical coupling and optical feedback, giving rise to a wealth of related phenomena [1,2]. Various different coupling schemes for lasers have been investigated. These include integrated photonic circuits [3–5], optical fiber networks [6,7], topological insulator vertical-cavity laser arrays [8], and various free-space approaches [9–12]. Applications exploiting the behavior of such (self-) coupled lasers include: 1) phase-locking to increase output powers via coherent beam combining [3]; 2) secure communications [13–15]; 3) random-bit generation [16–19]; and 4) brain-inspired computing [20,21] – for which possible extensions towards multiple lasers have been proposed [22].

However, to our best knowledge, there has been only one experimental realization [12] of optical coupling of SLs with significant strength within a scalable [23,24] and partially reconfigurable approach. Here, as in [12], we use diffractive optics in an external cavity to couple vertical-cavity surface-emitting lasers (VCSELs) in an array and to lock them to an external drive laser. The VCSELs in the custom-manufactured 5×5 square lattice array can be individually addressed via electrical biasing, allowing us to control the spectral detuning among individual emitters [25]. For 22 VCSELs, we achieve simultaneous optical injection locking to an external drive laser. Besides, without the external drive laser, we observe mutual locking of 22 VCSELs to a common wavelength and with strongly suppressed autonomous dynamics. In summary, we go beyond the

results in [12] by providing direct measurements of optical injection locking for individual lasers and a quantitative analysis of the achieved coupling and injection strengths. The VCSELs' high spectral uniformity and matched emission polarization, in combination with improvements in the imaging setup, allow us to substantially increase the size of the VCSEL network from 7 to 22 lasers. These are promising results in the search for a scalable photonic laser-network platform.

2.   Experimental setup

For our experiments, we use custom-manufactured GaInAs quantum well VCSELs with an AlGaAs layer for the oxide apertures and AlGaAs/GaAs distributed Bragg reflector (DBR) mirrors to define the central optically $\lambda/2$-thick cavity [25]. The array used for our experiments consists of VCSELs that are arranged in a 5×5 square lattice with a pitch of $p \approx 80$ μm. They emit with a dominant fundamental transverse mode at $\lambda \approx 976$ nm and exhibit a high degree of homogeneity: spectrally (within ±0.1 nm at the respective thresholds), in polarization ($\sigma = 4.4°$ due to a slightly elliptical cross-section [25]), and regarding their threshold currents I_{th} (323 μA ± 26 μA when excluding 3 outliers). Every VCSEL is individually electrically contacted and thus individually addressable, in our case with an 8-bit bias current resolution. In the following, we will refer to the VCSEL in column c and row r of the array as VCSEL (c, r).

Our diffractive coupling scheme, depicted in Fig. 1, and discussed in detail in [12,23,24], is based on an external cavity, which is comprised of a microscope objective (MO, Olympus LCPLN20XIR, $f_{MO} = 9$ mm, NA = 0.45), a diffractive optical element (DOE, Holoor MS-261-970-Y-X), an achromatic lens (L1, Thorlabs AC254-080-B, $f_{AC} = 80$ mm) and a broadband dielectric mirror (Thorlabs BB1-E03). The MO collimates the light before passing the DOE, the lens focuses the laser's emission on the external cavity mirror while the DOE spatially multiplexes the light. In our double-pass configuration, the 0th and higher diffractive orders form a 5×5 pattern, which is imaged back onto the array, where the 0th order overlaps with the aperature of the respective source laser and the higher diffractive orders overlap with the aperatures of the corresponding nearest and second-nearest neighboring VCSELs. This establishes a bidirectional coupling with a strength that decreases with the lattice-distance between the two involved VCSELs. The reflection at the 50/50 non-polarizing beam splitter cube (BS1, Thorlabs BS014) is used for measurement and analysis, as described further below.

The spatial multiplexing implemented via the DOE also allows for optically injecting an external edge-emitting DBR injection/drive laser diode (Thorlabs DBR976PN) into all 25 VCSELs simultaneously. This DBR laser is butt-coupled to a polarization-maintaining (PM) single-mode (SM) fiber and an optical isolator (iso). Its light is collimated using an aspheric lens (L2, Thorlabs AL1225-B, $f = 25$ mm, NA = 0.23) and polarization-aligned to the VCSELs using a $\lambda/2$ wave plate (Thorlabs WPH10M-980). This optical drive is injected into the external cavity using the reflection at BS1. By double-passing the DOE, it is spatially multiplexed similar to the beam of the central VCSEL and thus injected into all the VCSELs simultaneously, although the optical power is not equally distributed.

The VCSEL and DBR laser signals in the analysis branch are split again by a 70R/30T non-polarizing beam splitter cube (BS2, Thorlabs BS023). The transmitted part is coupled into an SM fiber using an aspheric lens (L3, Thorlabs AL2018, $f = 18$ mm). After a 50/50 fiber splitter, the light is analyzed using an optical spectrum analyzer (OSA, Anritsu MS9710C, FWHM resolution = 50 pm) and an optical power meter. The reflected light is coupled into a multimode (MM) fiber using a plano-convex lens (L4, Thorlabs LA1027-B, $f = 35$ mm). The dynamic properties are characterized using a photodiode (PD, New Focus 1554-A-50, 10 kHz to 12 GHz 3-dB-bandwidth) and an electrical spectrum analyzer (ESA, Anritsu MS2667C, 9 kHz to 30 GHz).

3. External optical injection

For investigating the VCSELs' behavior under external optical injection, we first spectrally aligned 22 of the 25 VCSELs to $\lambda_{\text{VCSEL}} = 976.770\,\text{nm} \pm 10\,\text{pm}$. We compensated for inhomogeneous heating of the array caused by electrical biasing. The remaining spectral inhomogeneity of 10 pm is mainly due to the 8-bit pump current resolution. Three short circuits between pairs of VCSELs prevent the exact spectral alignment of the three remaining VCSELs. The average output power of the VCSELs, when spectrally aligned at λ_{VCSEL}, is $\overline{P}_{\text{VCSEL}} = (224 \pm 91)\,\mu\text{W}$. For recording the optical spectra shown in this section, an SM fiber that was connected to the OSA was positioned behind L4, since the position of the SM fiber behind L3 is needed as an alignment reference and can thus only collect the light of the array's central VCSEL (3,3). In Fig. 2(a), we show optical spectra of VCSEL (2,5) for different injection laser wavelengths λ_{inj}. We tuned λ_{inj} by varying the injection laser temperature T_{inj}, maintaining its bias current at $I_{\text{inj}} = 450\,\text{mA}$, which corresponds to an optical output power $P_{\text{inj}} \approx 17\,\text{mW}$ after the optical isolator, of which $P_{\text{inj}}\big|_{\text{tf}(2,5)} = 94\,\mu\text{W}$ reach the top facet of VCSEL (2,5). Due to reflections at the VCSEL's top facet, the emission of the injection laser is also visible in the recorded optical spectrum.
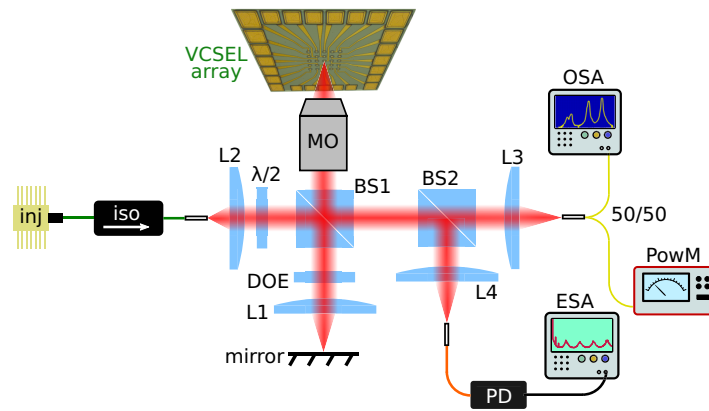

Fig. 1. Scheme of the experimental setup. An external cavity is formed by a microscope objective (MO), a lens (L1) and a mirror. A diffractive optical element (DOE) creates multiple beams, establishing coupling between VCSELs and enabling simultaneous optical injection into all the VCSELs of the array. The injection branch consists of a DBR injection laser (inj), an optical isolator (iso), an aspheric lens (L2) and a half-wave plate ($\lambda/2$). Via reflection at a 50/50 beam splitter (BS1), the injected signal enters the external cavity and the VCSEL signal enters the analysis branch, which contains a 70R/30T beam splitter (BS2), an aspheric (L3) and a plano-convex lens (L4), a fiber splitter (50/50), an optical spectrum analyzer (OSA), a powermeter (PowM), a photodiode (PD), and an electrical spectrum analyzer (ESA).

For all but the central VCSEL (due to cross-talk from the injection laser), we observe side-mode suppression and/or a shift of the VCSEL's spectral peak to λ_{inj}. These are signatures of optical injection locking. We determine the width of the injection-locking region with two different methods. First, we consider a VCSEL locked to the injection laser via its fundamental emission mode, when the VCSEL's next higher laterally confined emission mode is suppressed by at least 5 dB due to the injection. We define the upper boundary of the resulting injection locking region as $\lambda_{\text{inj,msps}}$, which is indicated by a dashed green line in Fig. 2(a). The related detuning is $\Delta\lambda_{\text{lock}} = \lambda_{\text{inj,msps}} - \lambda_{\text{VCSEL}}$, and the values are given on the left in Table 1. This allows us to identify such locking for 21 of 24 non-central VCSELs. For the remaining 3 VCSELs, the side-modes were too weak or their suppression was not sufficiently strong to provide a clear result.
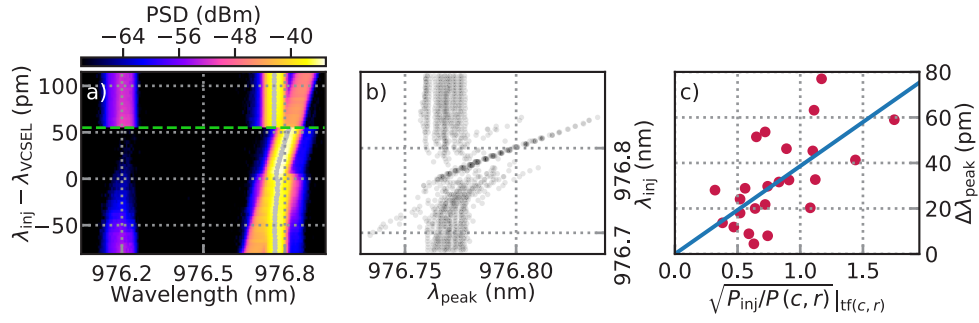
Fig. 2. a) Stacked color-coded spectra of VCSEL (2,5) under injection of an external drive laser at different injection laser wavelengths λ_{inj}. Grey trace: Spectral peaks (λ_{peak}), obtained as midpoints between −3 dB crossings around point of maximal power spectral density (PSD). Dashed green line: $\Delta\lambda_{\text{lock}}$, i.e. highest detuning between injection laser and VCSEL at which the side-mode is suppressed by ≥ 5 dB. b) Spectral peaks (λ_{peak}) of 21 injection-locked VCSELs at different λ_{inj}. c) Plot of $\Delta\lambda_{\text{peak}}$ vs. the expected ratio of injection laser power (P_{inj}) and VCSEL power ($P(c, r)$) at the surface of the different VCSELs (c, r). Blue line: Linear fit through zero.

Thus, we use a second method, which analyzes the wavelength of the peak with the highest power spectral density (PSD), λ_{peak}, as a function of λ_{inj}. For this, we smoothed the data using a 2$^{\text{nd}}$ order binomial filter and then calculated the midpoint between the −3 dB crossings at both sides of the peak. We plot λ_{peak} as gray dots, cf. Fig. 2(a), and against λ_{inj} for all the VCSELs of the array, cf. Fig. 2(b). We observe that the slightly spectrally inhomogeneous VCSELs collapse onto λ_{inj} nearly simultaneously in the region of injection locking. Note that in some spectra in Fig. 2(b), artifacts arise from the superposition of injection laser and VCSEL spectra. The maximal detunings $\Delta\lambda_{\text{peak}} = \max(\lambda_{\text{peak}} - \lambda_{\text{VCSEL}})$ are given in Tab. 1 on the right.

Table 1. Right: maximal shift of the spectral maximum due to optical injection locking to the external laser, obtained from −3 dB crossings ($\Delta\lambda_{\text{peak}}$). Left: highest detuning between VCSEL and external laser at which the side-mode was suppressed by at least 5 dB ($\Delta\lambda_{\text{lock}}$). We observe good agreement between both sets of values.

$\Delta\lambda$ (pm)	(1,*)	(2,*)	(3,*)	(4,*)	(5,*)
(*,1)	15/14	22/20	-/59	9/8	16/18
(*,2)	26/24	33/33	62/62	33/33	-/5
(*,3)	51/51	45/45	-	41/41	34/32
(*,4)	29/29	45/46	75/76	-/20	11/9
(*,5)	29/28	53/53	23/22	32/33	14/12

From the listed $\Delta\lambda_{\text{peak}}$, we determine the average coupling coefficient for injection. For most VCSELs, $\Delta\lambda_{\text{peak}}$ is close to $\Delta\lambda_{\text{lock}}$. This justifies the use of $\Delta\lambda_{\text{peak}}$ as a measure for the injection locking window, which is given by [26–28]

$$-k_c \sqrt{1 + \alpha^2} \left. \sqrt{\frac{P_{\text{inj}}}{P(c, r)}} \right|_{\text{tf}(c,r)} \leq \Delta\omega \leq k_c \left. \sqrt{\frac{P_{\text{inj}}}{P(c, r)}} \right|_{\text{tf}(c,r)}, \tag{1}$$

where $\Delta\omega = 2\pi(f_{\text{inj}} - f(c, r))$ is the difference of the angular frequencies between drive laser and VCSEL (c, r); α and $P(c, r)$ are the VCSEL's linewidth enhancement factor and its output power,

respectively, and $P_{\text{inj}}\big|_{\text{tf}(c,r)}$ is the power of the injection laser at the top facet of the VCSEL and k_c is the coupling coefficient of the injection laser into the VCSELs. We know that $k_c \propto \tau_c^{-1}$ [27], with τ_c being the cavity photon lifetime. From Eq. (1), we derive

$$\Delta\lambda_{\text{peak}}(c,r) = \frac{\lambda^2}{2\pi c} k_c \sqrt{1 + \alpha^2} \left. \sqrt{\frac{P_{\text{inj}}}{P(c,r)}}\right|_{\text{tf}(c,r)} \tag{2}$$

at the upper injection locking boundary. We inserted $\Delta\omega = -2\pi c\Delta\lambda/\lambda^2$, where $\Delta\lambda = c/f_{\text{inj}} - c/f(c,r)$ and $\lambda = c/f_{\text{inj}} \approx c/f(c,r)$. $P_{\text{inj}}\big|_{\text{tf}(c,r)}$ can be expressed as

$$P_{\text{inj}}\big|_{\text{tf}(c,r)} = T_{\text{MO}} T_{\text{BS1}} R_{\text{BS1}} C_{\text{DOE}}(c,r) P_{\text{inj}}, \tag{3}$$

where P_{inj} is the optical power of the injection laser after the optical isolator, $T_{\text{MO}} = 0.9$, $T_{\text{BS1}} = 0.48$, and $R_{\text{BS1}} = 0.46$ are the transmission and reflection coefficients of MO and BS1, respectively, and $C_{\text{DOE}}(c,r)$ is the DOE's multiplexing matrix coefficient for VCSEL (c,r), which ranges from 1/81 for the corner VCSELs (1,1), (1,5), (5,1), and (5,5) to 1/9 for the central VCSEL (3,3). In Fig. 2(c), the maximal $\Delta\lambda_{\text{peak}} = \lambda_{\text{peak}} - \lambda_{\text{VCSEL}}$ for each VCSEL (c,r) is plotted versus $\sqrt{P_{\text{inj}}/P(c,r)}\big|_{\text{tf}(c,r)}$ with a linear fit, from which we obtain a slope of 39 pm. Using Eq. (2), we obtain $15\,\text{ns}^{-1} < k_{c,\text{inj}} < 35\,\text{ns}^{-1}$ as an estimate for the coupling coefficient for injection, assuming $2 < \alpha < 5$. This is comparable to the range of $30\,\text{ns}^{-1} \lessapprox k_c \lessapprox 40\,\text{ns}^{-1}$, which we obtain as an estimate from [29] for the injection via optical fibers into VCSELs that emit at 1550 nm.

Finally, we demonstrate simultaneous injection locking of 22 out of 25 VCSELs in the array. For this, we first fine-adjusted the pump currents to maximize side-mode suppression and peak shift. Then, we recorded optical spectra for every VCSEL in three different configurations, keeping the VCSELs' bias currents and T_{inj} constant. As shown for three examples in Fig. 3, in 21 out of 24 cases, we observed side-mode suppression and/or a shift of the spectral maximum with optical injection, compared to the solitary VCSEL with and without feedback. Since the central VCSEL receives the largest portion of the injected light and is spectrally aligned, we assume that it is injection-locked as well, although due to cross-talk from the injection laser this is impossible to verify.
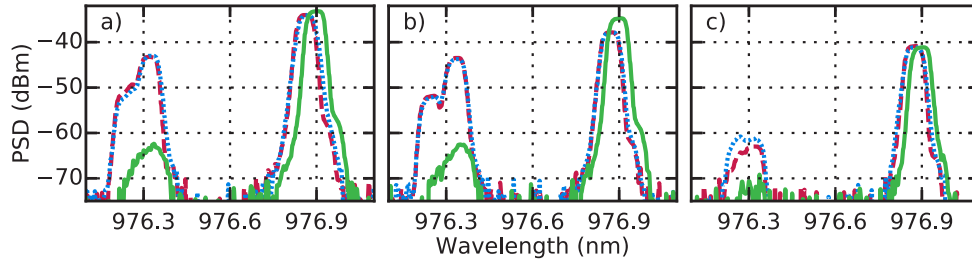

Fig. 3. Optical spectra of three different VCSELs in three different configurations each. Dashed red lines correspond to blocking the external cavity, allowing for neither feedback nor injection. Dotted blue lines correspond to blocking the injection path, but not the feedback. Solid green lines correspond to a configuration with both feedback and injection. a) VCSEL (1,4), b) VCSEL (3,5), c) VCSEL (4,5).

4.   Pairwise coupling

We limit our study to pairwise interactions between the central VCSEL (3,3) and one other VCSEL (c,r), as investigating all 231 possible pairwise interactions between independently

controllable VCSELs would be unrealistic. Note that VCSEL (3,1) is short-circuited with the central VCSEL (3,3) and thus also always switched on. The other two pairs of short-circuited VCSELs are (2,1) & (3,2) and (4,1) & (5,1). Importantly, due to the large wavelength detuning at identical current of the short-circuited pairs, the coupling was not perturbed by the other laser of the pair that was not investigated. In our measurements, we increased $I(c, r)$ while keeping $I(3, 3) = 0.4\,\text{mA} = 1.3\,I_{\text{th}}$ constant and with all the other VCSELs switched off. At every step, we recorded the optical and the radio-frequency (RF) spectrum of VCSEL (3,3). For the pairwise interactions with VCSELs (3,4) and (2,4), these data are shown in Fig. 4(a)–(d), plotted against $\lambda(c, r) - \lambda(3, 3)$ at the respective bias currents $I(c, r)$. Due to reflections, contributions from the second VCSEL are visible in addition to the signal from the central VCSEL. For more than half of the VCSELs, we observe a shift of the central VCSEL to $\lambda(c, r)$, due to its spectral locking with the other laser [30]. Furthermore, in the RF spectra, we always observe a signature for pairwise interaction, even for the cases where no clear signature can be found in the optical spectra, see Fig. 4(c) and (d). Although these signatures differ for coupling to different VCSELs, in nearly all the cases, at the boundary of the locking region, we observe an increased PSD around the two peaks at 2.6 GHz and 3.1 GHz that were previously present with feedback. There are two more phenomena that we observe in about half of the cases, not necessarily occurring at the same time. Inside the locking region, we observe a suppression of the two peaks at 2.6 GHz and 3.1 GHz, and, at the edge of the locking region, we observe the appearance of multiple peaks at frequencies above 3 GHz, which are about one external cavity frequency apart.
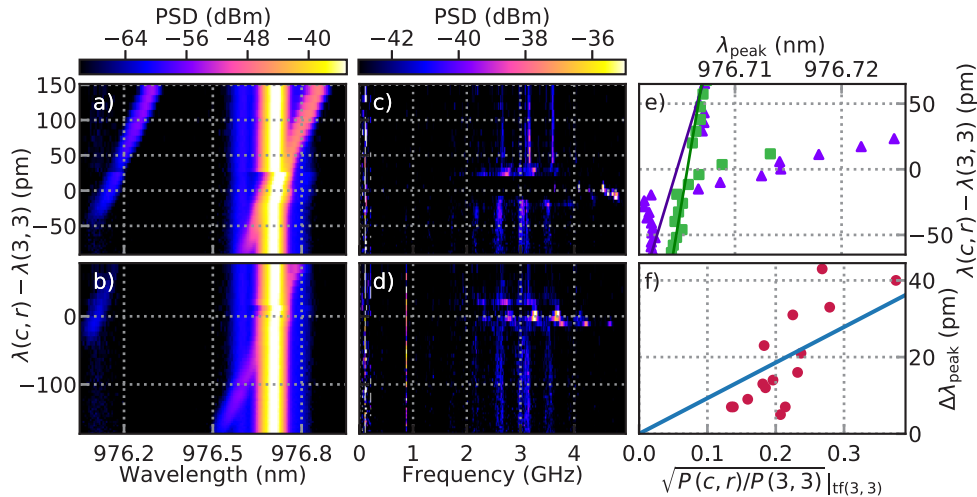

Fig. 4. a) Optical spectra of VCSEL (3,3) when tuning the wavelength of VCSEL (3,4), $\lambda(3, 4)$. b) Optical spectra of VCSEL (3,3) when tuning $\lambda(2, 4)$. Both with the rest of the VCSELs switched off. c) RF spectra corresponding to a). d) RF spectra corresponding to b). e) Peak positions (λ_{peak}) as extracted from a) (violet triangles) and b) (green squares). Lines: linear fits to the points far from the injection locking region. f) Maximal peak shift $\Delta\lambda_{\text{peak}} = \max(\lambda_{\text{peak}} - \lambda(3, 3))$ as observed in the optical spectrum of VCSEL (3,3) for coupling with different VCSELs plotted vs. expected ratio of powers of VCSEL (3,3) and other VCSEL at the surface of VCSEL (3,3). Line: linear fit through zero.

To quantify the mutual locking, we extract λ_{peak} from the optical spectra, as explained in the previous section. For VCSELs (3,4) and (2,4), i.e. for the data from Fig. 4(a) and (b), λ_{peak} is plotted in Fig. 4(e) as a function of the detuning. Since $\lambda(3, 3)$ slightly increases with $I(c, r)$ due to heating of the array, we interpolate $\lambda(3, 3)$ by linearly fitting the points far from the locking region. We then determine $\Delta\lambda_{\text{peak}} = \max(\lambda_{\text{peak}} - \lambda(3, 3))$ for each VCSEL. Similar to Eq. (2),

we calculate the optical power of VCSEL (c, r) at the top facet of VCSEL (3,3) by

$$P(c,r)|_{\text{tf}(3,3)} = T_{\text{MO}}^2 T_{\text{BS1}}^2 C_{\text{DOE}}(c,r)P(c,r). \tag{4}$$

In Fig. 4(f), $\Delta\lambda_{\text{peak}}$ for each VCSEL is plotted against $\sqrt{P(c,r)/P(3,3)}\Big|_{\text{tf}(3,3)}$. Again, we linearly fit the data and obtain a slope of 32 pm. Thus, we arrive at $13\,\text{ns}^{-1} < k_{\text{c,pair}} < 29\,\text{ns}^{-1}$ as an estimate for the pairwise coupling coefficient, which is about 20% lower than for injection from the external drive laser. Notably, the precision of these measurements is limited by the 50 pm FWHM resolution of the OSA.

5. Entire array coupling

To investigate the mutual coupling of the entire array, we kept $I(3,3) = 0.4\,\text{mA}$ constant and simultaneously tuned the pump current of all non-central VCSELs, keeping the tuned VCSELs maximally spectrally homogeneous. At every step, we recorded an optical and an RF spectrum of VCSEL (3,3), see Fig. 5. Due to reflections at the top facet of VCSEL (3,3), contributions of the other VCSELs are visible in the spectra. To minimize cross-talk due to array heating, we experimentally determined $\lambda(3,3)$ at every step by temporarily blocking the external cavity and recording the optical spectra, thus avoiding reflections and optical injection locking effects. We also experimentally determined λ_{nc}, the spectral peak of the ensemble of the non-central VCSELs, by recording spectra with VCSEL (3,3) switched off, i.e. the summed spectra of all the non-central VCSELs' emissions through their reflection at the top facet of VCSEL (3,3).
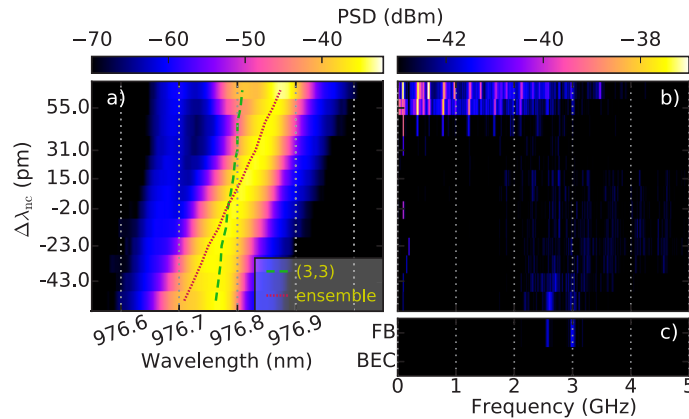

Fig. 5. Color-coded spectra of VCSEL (3,3) at $I(3,3) = 0.4\,\text{mA} = 1.3\,I_{\text{th}}$ coupled to the entire array. The y-axis represents the spectral detuning $\Delta\lambda_{\text{nc}} = \lambda_{\text{nc}} - \lambda(3,3)$. a) Optical spectra. Red dotted line: spectral maximum λ_{nc} of the ensemble of the non-central VCSELs. Green dashed line: $\lambda(3,3)$. The near-vertical blue trace at about 976.7 nm stems from VCSEL (3,1), which is short-circuited with VCSEL (3,3) and can thus not be tuned independently. b) Corresponding RF spectra. c) RF spectra of solitary VCSEL (3,3) with feedback ('FB') and blocked external cavity ('BEC').

We observe a clear transition in both optical and RF spectra upon increasing $\Delta\lambda_{\text{nc}} = \lambda_{\text{nc}} - \lambda(3,3)$. Two more datasets showing similar behavior have been recorded. In Fig. 5, the main transition occurs between $\Delta\lambda_{\text{nc}} = 47\,\text{pm}$ and $\Delta\lambda_{\text{nc}} = 55\,\text{pm}$. In the optical spectra, for $\Delta\lambda_{\text{nc}} \leq 47\,\text{pm}$, VCSEL (3,3) is optically locked with the rest of the VCSELs before the previously suppressed peak at $\lambda(3,3)$ reappears for $\Delta\lambda_{\text{nc}} \geq 55\,\text{pm}$. In the RF spectra, peaks and an increased floor appear at frequencies below 3 GHz for $\Delta\lambda_{\text{nc}} \geq 55\,\text{pm}$. We expect residual wavelength inhomogeneities between different VCSELs due to the 8-bit pump current resolution to be up to 0.01 nm, which

corresponds to up to 3 GHz. Thus, we interpret the peaks that appear in the RF spectra for $\Delta\lambda_{nc} \geq 55$ pm as beating between different VCSELs. Since this beating appears at the same time as the unlocking of VCSEL (3,3), we conclude that all 22 independently tunable VCSELs are mutually optically locked for $\Delta\lambda_{nc} \leq 47$ pm.

Again, we estimate the coupling coefficient using $\Delta\lambda_{nc} = 47$ pm as the upper locking boundary, and $\sum_{(c,r)} P(c,r)|_{tf(3,3)} /P(3,3) \approx 1.14$ as the power ratio, similar to Eq. (4). With these values, we obtain a coupling coefficient comparable to $k_{c,inj}$ and $k_{c,pair}$. Since Eq. (1) assumes a single monochromatic source and not several VCSELs with uncorrelated phases, one would expect the coupling coefficient for entire array coupling (incomplete locking) to be smaller than the one for pairwise coupling. That this is not the case corroborates our claim of entire array locking. Importantly, we do not find the same unlocking characteristics in the RF spectra for negative frequency detuning. We assign this predominantly to the fact that the emission power of all VCSELs is around 5 dB lower at the estimated lower boundary of the emission region than at the upper one. This is comparable to the dynamic range of the RF spectra shown in Fig. 5. Please note that we do not expect this to affect the detection of the upper locking boundary, because the difference in output power between $\Delta\lambda_{nc} = 0$ pm and $\Delta\lambda_{nc} = 47$ pm is only around 1.5 dB.

6. Conclusion

In conclusion, we present results on optical injection and diffractive coupling of VCSELs in a 5×5 square lattice array. For all individual VCSELs, we achieve optical injection locking to an external drive laser and determine a coupling coefficient of $15\,\text{ns}^{-1}<k_{c,inj}<35\,\text{ns}^{-1}$. Furthermore, we achieve simultaneous optical injection locking of 22 out of the 25 array VCSELs to the external drive laser. Based on the central VCSEL's RF spectra, we show clear signatures of pairwise coupling between the central and all other VCSELs of the array and demonstrate pairwise optical locking for 13 out of 21 VCSELs/pairs of short-circuited VCSELs. We estimate a coupling coefficient of $13\,\text{ns}^{-1}<k_{c,pair}<29\,\text{ns}^{-1}$, the precision of which is limited by the resolution of the OSA and the low power ratio between the different VCSELs. This is comparable to values for injection into VCSELs via an optical fiber [29]. When coupling the entire array, we observe a simultaneous transition in both optical and RF spectra of the central VCSEL. We interpret this as a transition from optical locking of the entire array to unlocking.

Our findings show that custom-engineered VCSEL arrays with external diffractive optical coupling are feasible platforms for realizing large-scale networks of SLs, since the coupling concept can be scaled to substantially larger arrays using a similar DOE [23,24]. In general, large-scale laser networks show potential for applications in laser machining and lighting. They are also of interest for experimentally studying fundamental properties of complex systems. Last but not least, they offer attractive properties for optical machine learning. Our results demonstrate that the obtained coupling between the VCSELs creates a network. Although, in our network, the coupling strengths between different laser pairs are not independently tunable, this could be achieved to a certain degree by replacing the external cavity mirror with a spatial light modulator (SLM). Moreover, optical injection locking to an external drive laser can be achieved, enabling information injection into the system. Finally, trainable readout weights can be readily implemented using an SLM [24]. This would create a fully hardware-implemented and parallel photonic neural network with correspondence of one laser per artificial neuron and potentially high-bandwidth operation.

Disclosures. The authors declare no conflicts of interest.

Data availability. Data underlying the results presented in this paper are not publicly available at this time, but may be obtained from the authors upon reasonable request.

References

1. S. Wieczorek, B. Krauskopf, T. Simpson, and D. Lenstra, "The dynamical complexity of optically injected semiconductor lasers," Phys. Rep. **416**(1-2), 1–128 (2005).
2. M. C. Soriano, J. García-Ojalvo, C. R. Mirasso, and I. Fischer, "Complex photonics: Dynamics and applications of delay-coupled semiconductors lasers," Rev. Mod. Phys. **85**(1), 421–470 (2013).
3. Z. Gao, B. J. Thompson, G. Ragunathan, M. T. Johnson, B. Rout, and K. D. Choquette, "Bottom-Emitting Coherently Coupled Vertical Cavity Laser Arrays," IEEE Photonics Technol. Lett. **28**(4), 513–515 (2016).
4. T. Y. Kao, J. L. Reno, and Q. Hu, "Phase-locked laser arrays through global antenna mutual coupling," Nat. Photonics **10**(8), 541–546 (2016).
5. L. Bao, N.-H. Kim, L. Mawst, N. Elkin, V. Troshchieva, D. Vysotsky, and A. Napartovich, "Modeling, fabrication, and characterization of large aperture two-dimensional antiguided vertical-cavity surface-emitting laser arrays," IEEE J. Sel. Top. Quantum Electron. **11**(5), 968–981 (2005).
6. M. Hill, E. Frietman, H. de Waardt, G.-D. Khoe, and H. Dorren, "All fiber-optic neural network using coupled SOA based ring lasers," IEEE Trans. Neural Netw. **13**(6), 1504–1513 (2002).
7. A. Argyris, M. Bourmpos, and D. Syvridis, "Experimental synchrony of semiconductor lasers in coupled networks," Opt. Express **24**(5), 5600–5614 (2016).
8. A. Dikopoltsev, T. H. Harder, E. Lustig, O. A. Egorov, J. Beierlein, A. Wolf, Y. Lumer, M. Emmerling, C. Schneider, S. Höfling, M. Segev, and S. Klembt, "Topological insulator vertical-cavity laser array," Science **373**(6562), 1514–1517 (2021).
9. T. Heil, I. Fischer, W. Elsässer, J. Mulet, and C. Mirasso, "Chaos Synchronization and Spontaneous Symmetry-Breaking in Symmetrically Delay-Coupled Semiconductor Lasers," Phys. Rev. Lett. **86**(5), 795–798 (2001).
10. I. Fischer, R. Vicente, J. M. Buldú, M. Peil, C. R. Mirasso, M. C. Torrent, and J. García-Ojalvo, "Zero-lag long-range synchronization via dynamical relaying," Phys. Rev. Lett. **97**(12), 123902 (2006).
11. M. Nixon, M. Fridman, E. Ronen, A. A. Friesem, N. Davidson, and I. Kanter, "Controlling synchronization in large laser networks," Phys. Rev. Lett. **108**(21), 214101 (2012).
12. D. Brunner and I. Fischer, "Reconfigurable semiconductor laser networks based on diffractive coupling," Opt. Lett. **40**(16), 3854–3857 (2015).
13. H. Koizumi, S. Morikatsu, H. Aida, T. Nozawa, I. Kakesu, A. Uchida, K. Yoshimura, J. Muramatsu, and P. Davis, "Information-theoretic secure key distribution based on common random-signal induced synchronization in unidirectionally-coupled cascades of semiconductor lasers," Opt. Express **21**(15), 17869–17893 (2013).
14. X. Porte, M. C. Soriano, D. Brunner, and I. Fischer, "Bidirectional private key exchange using delay-coupled semiconductor lasers," Opt. Lett. **41**(12), 2871–2874 (2016).
15. Q. Li, S. Lu, Q. Bao, D. Chen, M. Hu, R. Zeng, G. Yang, and S. Li, "Simultaneously bidirectional transmission of message between three coupled semiconductor lasers," Opt. Commun. **423**, 155–161 (2018).
16. A. Uchida, K. Amano, M. Inoue, K. Hirano, S. Naito, H. Someya, I. Oowada, T. Kurashige, M. Shiki, S. Yoshimori, K. Yoshimura, and P. Davis, "Fast physical random bit generation with chaotic semiconductor lasers," Nat. Photonics **2**(12), 728–732 (2008).
17. N. Oliver, M. C. Soriano, D. W. Sukow, and I. Fischer, "Fast random bit generation using a chaotic laser: Approaching the information theoretic limit," IEEE J. Quantum Electron. **49**(11), 910–918 (2013).
18. R. Sakuraba, K. Iwakawa, K. Kanno, and A. Uchida, "Tb/s physical random bit generation with bandwidth-enhanced chaos in three-cascaded semiconductor lasers," Opt. Express **23**(2), 1470–1490 (2015).
19. Y. Guo, Q. Cai, P. Li, R. Zhang, B. Xu, K. A. Shore, and Y. Wang, "Ultrafast and real-time physical random bit extraction with all-optical quantization," Adv. Photonics **4**(03), 1–8 (2022).
20. D. Brunner, M. C. Soriano, C. R. Mirasso, and I. Fischer, "Parallel photonic information processing at gigabyte per second data rates using transient states," Nat. Commun. **4**(1), 1364 (2013).
21. J. Vatin, D. Rontani, and M. Sciamanna, "Experimental reservoir computing using VCSEL polarization dynamics," Opt. Express **27**(13), 18579–18584 (2019).
22. C. Sugano, K. Kanno, and A. Uchida, "Reservoir Computing Using Multiple Lasers with Feedback on a Photonic Integrated Circuit," IEEE J. Sel. Top. Quantum Electron. **26**(1), 1–9 (2020).
23. S. Maktoobi, L. Froehly, L. Andreoli, X. Porte, M. Jacquot, L. Larger, and D. Brunner, "Diffractive Coupling For Photonic Networks: How Big Can We Go?" IEEE J. Sel. Top. Quantum Electron. **26**(1), 1–8 (2020).
24. J. Bueno, S. Maktoobi, L. Froehly, I. Fischer, M. Jacquot, L. Larger, and D. Brunner, "Reinforcement Learning in a large scale photonic Recurrent Neural Network," Optica **5**(6), 756–760 (2018).
25. T. Heuser, M. Pflüger, I. Fischer, J. A. Lott, D. Brunner, and S. Reitzenstein, "Developing a photonic hardware platform for brain-inspired computing based on 5×5 VCSEL arrays," J Phys Photonics **2**(4), 044002 (2020).
26. C. H. Henry, N. A. Olsson, and N. K. Dutta, "Locking Range and Stability of Injection Locked 1.54 µm InGaAsP Semiconductor Lasers," IEEE J. Quantum Electron. **21**(8), 1152–1156 (1985).
27. J. Ohtsubo, *Semiconductor Lasers: Stability, Instability and Chaos* (Springer, 2013), p. 173, 3rd ed.
28. C.-H. Chang, L. Chrostowski, and C. Chang-Hasnain, "Injection locking of VCSELs," IEEE J. Sel. Top. Quantum Electron. **9**(5), 1386–1393 (2003).

29. A. Hurtado, D. Labukhin, I. D. Henning, and M. J. Adams, "Injection locking bandwidth in 1550-nm vcsels subject to parallel and orthogonal optical injection," IEEE J. Sel. Top. Quantum Electron. **15**(3), 585–593 (2009).

30. H.-J. Wünsche, S. Bauer, J. Kreissl, O. Ushakov, N. Korneyev, F. Henneberger, E. Wille, H. Erzgräber, M. Peil, W. Elsässer, and I. Fischer, "Synchronization of delay-coupled oscillators: A study of semiconductor lasers," Phys. Rev. Lett. **94**(16), 163901 (2005).